CHAPTER 5

ADSORPTION MECHANISM OF NICKEL DECORATED α-CN MONOLAYER TOWARDS CO, NO, AND NH_3 GASES

5.1. INTRODUCTION

As per the discussion in chapter-1, industrial incinerations and incomplete combustions are major sources of toxic gases, mainly carbon monoxide (CO) and nitric oxide (NO). These gases, being colorless and odorless, pose grave threats to human health and the environment[1]. In recent times, CO poisonings from radiators have emerged as a pertinent issue. When inhaled, CO combines with hemoglobin to form carboxy-hemoglobin, reducing the blood's oxygen-carrying capacity. This leads to oxygen displacement in the blood, starving vital organs and causing suffocation and loss of consciousness[2]. Similarly, exposure to nitrogen oxides primarily occurs through inhalation, though systemic effects can result from exposure via any route. Nitrogen oxides irritate the eyes, skin, mucous membranes, and respiratory tract[3]. Despite its role in green hydrogen production, the potential hazards of ammonia (NH_3) cannot be disregarded due to its corrosive nature[4]. The severity of health effects depends on exposure route, dose, and duration. High concentrations of airborne ammonia cause immediate burning of the eyes, nose, throat, and respiratory tract, potentially resulting in blindness, lung damage, or death[5]. While monitors for toxic gases such as carbon monoxide are available in the market[6], their high price range relative to the purchasing power parity (PPP) in countries like India presents a challenge[7]. Hence, the quest for novel and cost-effective materials for toxic gas sensing devices remains relentless.

Two-dimensional materials such as Graphene[8], have been explored for multi-faceted applications. This is attributed to the high surface-to-volume ratio, numerous potential interaction sites and material sensitivity of the said materials. When it comes to the toxic gas adsorption mechanisms, 2D materials have indeed undergone thorough examination for their potential applications[11]. However, the adsorption mechanisms of pristine monolayers possess some challenges. For example, density functional theory (DFT) analysis of graphene, unveiled its capability in detecting toxic gas molecules, showcasing a weak interaction (physisorption) between them[12]. Nevertheless, with the introduction of transition metals such as Ni, Pd, and Pt as decoration, the gas adsorption experiences substantial enhancement.[13] Hexagonal boron nitride (h-BN) stands out as another prominent 2D material investigated for its adsorption mechanisms. One notable instance involves the utilization of Ni-decoration on h-BN, which serves to catalyze the adsorption of hydrogen[14]. In addition to the Ni-atom, the use of Pd and Pt decoration has proven effective in improving the gas sensing performance of one-dimensional carbon nanotubes[15]. Moreover, multiple transition metal impurities have been embedded within MoS_2 monolayers to explore their gas adsorption performances[16]. Nickel,

employed as an impurity, has been integrated into different materials for gas adsorption applications. This includes doped MoS_2 and C_3N monolayers, ZIF-8 clusters, and ZnO surfaces, all featuring nickel impurity [17,18,19,20]. Furthermore, previous studies have investigated the application of carbon nanotubes (CNTs) doped with nickel for the detection of gases dissolved in oil [21].

In 2018, using first-principles density functional theory (DFT) calculations, Özdamar et al. investigated a family of stable two-dimensional crystals with the chemical formula A_2B_2 where *A* and *B* belong to groups IV and V, respectively (A = C, Si, Ge, Sn, Pb; B = N, P, As, Sb, Bi). They demonstrated that two structural symmetries of hexagonal lattices are dynamically stable, named as the α- and β-phases. In this paper, they predicted that the α-phase C_2N_2 or simply α-CN, is suitable for adsorption mechanisms such as hydrogen evolution, among other potential applications. Following this prediction, researchers explored the application of the pristine and doped α-CN monolayer for the full water splitting reaction [22]. Furthermore, an in-depth analysis using DFT calculations showcased the thermoelectric properties of α-CN and α-CP monolayers [23]. Recently, He et al. conducted a study on the interaction of various pollutant gases, including CO_2, CO, NO_2, H_2, NH_3, N_2, O_2, CH_4, and SO_2, with the α-CN monolayer [24]. Building upon this groundwork, our previous study investigated the pristine, Al-doped, and defected α-CX (X = N, P) monolayers for the adsorption of CO and NO gases [25].

One potential research gap that stands out from the passages above, is the need for more comprehensive studies exploring the synergistic effects of transition metal impurities in enhancing the gas adsorption mechanisms of 2D monolayers such as α-CN. Therefore, in this work, we have revisited the adsorption performance of α-CN monolayer with nickel decoration towards CO, NO, and NH_3 gas molecules. Our findings commence with the examination of variations in structural and electronic properties for Ni decorated α-CN. Then we explain the adsorption performance with the variation again in the structural parameters, electronic properties such as projected density of states (PDOS), band structure, as well as charge density diagrams and transfer mechanism. We have further computed sensing properties such as work function and recovery time. To further test the credibility of Ni doped α-CN as a sensing device material, we have performed a detailed conductivity analysis as well.

5.2.METHODOLOGY

To replicate the structural and electronic properties of α-CN monolayer, *ab-initio* DFT calculations were conducted using the Quantum Espresso package[26,27]. The exchange-correlation interaction was handled using the generalized gradient approximation-based pseudopotentials developed by Perdew-Burke-Ernzerhof [28]. The kinetic energy cutoff for the wave function was set at 70 Ry, ensuring full convergence of the total energy and structural parameters within the specified threshold. A 20 Å vacuum slab was included in the Z direction to minimize interaction between successive layers. Brillouin zone integration utilized a 7×7×1 K-mesh grid constructed using the Monkhorst-Pack scheme[29]. Van der Waals corrections, specifically Grimme DFT-D2, were applied to model the interaction between adsorbed gases and the monolayer. Necessary calculations employed the Marzari-Vanderbilt smearing technique. For the adsorption properties investigation, a 3×3×1 supercell of α-CN with Ni decoration, comprising 37 atoms, was considered. The adsorption energy was calculated using the equation[30]:

$$E_{ads} = E_{system+gas} - (E_{system} + E_{gas}) \text{ ---- (1)}$$

where $E_{system+gas}$ is the total energy of Ni-decorated α-CN with the adsorbed gas, E_{system} is the energy of Ni-decorated α-CN, and E_{gas} is the energy of CO, NO, and NH_3 molecules. A negative adsorption energy value indicates an exothermic process, suggesting stable adsorption of the gas molecules over the monolayer system.

Using the results from Quantum Espresso simulations, the electrical conductivity (σ_e/τ) was obtained through the BoltzTraP simulations [31]. The wave functions were recalculated using a substantially dense k-mesh grid of 24×24×1. The reason is that BoltzTraP calculations mainly rely on the wave-vector-dependent energy function. Using a denser k-mesh grid enhances the accuracy of the band structure and energy values related to the wave vector, thereby more accurately determining the carrier concentration and the consequent transport properties [32].

5.3.RESULTS AND DICUSSION

5.3.1. Structural and Electronic Properties of Ni-decorated α-CN monolayer

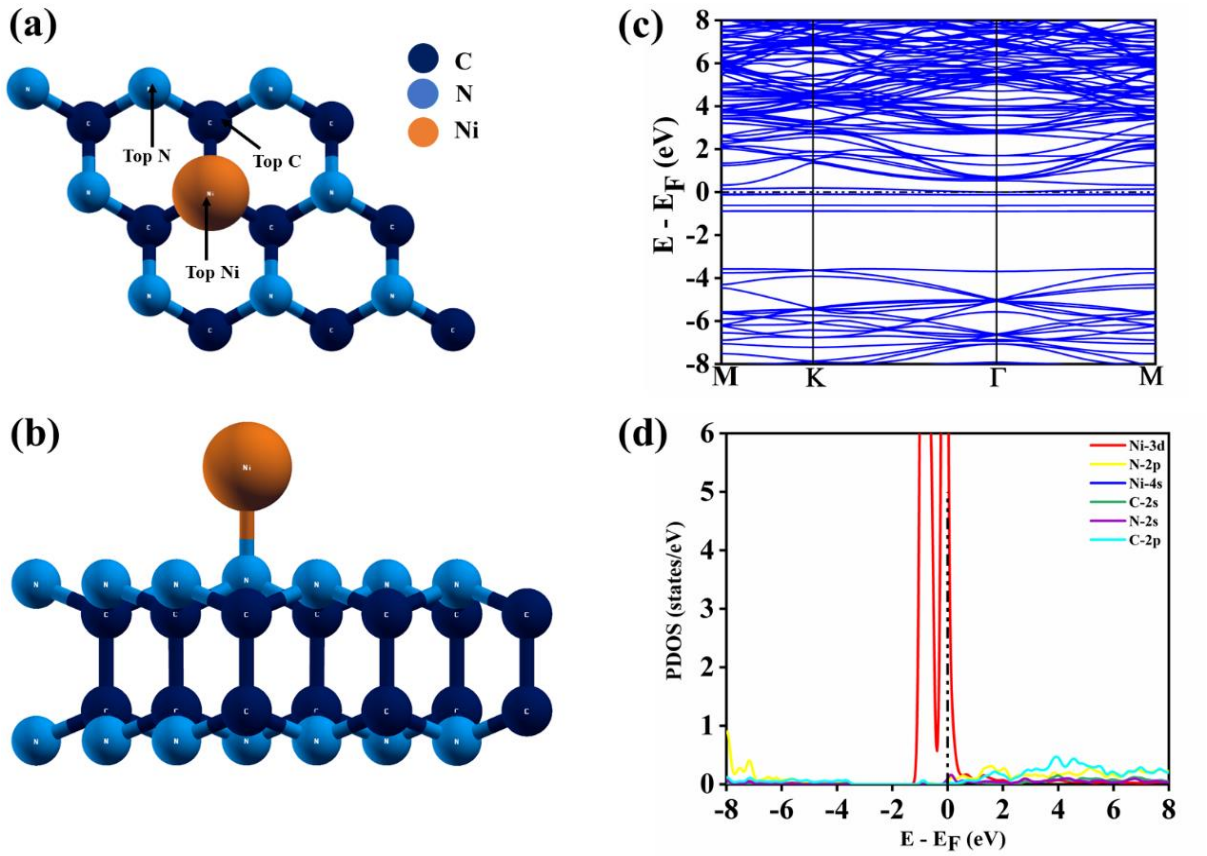

Figure 5.1: (a) Top view (b) side view (c) band structure (d) PDOS plot for Ni decorated α-CN

In order to enhance the adsorption performance, we decorated nickel (Ni) atom over the pristine α-CN monolayer. For the decoration of Ni atom, four potential sites were considered: the C-site, N-site, hollow site and top of the bridge. The N-site, being the energetically favourable system, was selected for further calculations. Upon Ni decoration, the average C-C bond length remains 1.63 Å, the N-N bond length becomes 2.63 Å, and Ni binds with the N atom at a distance of 1.89 Å, while being 3.67 Å apart from the nearest carbon atom. The average bond angle is 112° (see Fig. 5.1 (a) & (b)). The lattice parameter is 2.368 Å is similar as compared to that of the pristine monolayer [25]. α-CN semiconductor transitions to an extrinsic state upon Ni decoration, forming an intermediate band at the Fermi level, as evidenced by the band structure and PDOS shown in Fig. 5.1 (c) & (d). The PDOS plot shows the peak of 3d orbital of Ni atom to be highest indicating the strong covalent interaction between the impurity atom and the pristine monolayer [33,34].

5.3.2. Structural and electronic properties of gas adsorbed Ni decorated α-CN

For the Ni-decorated α-CN, among the three possible sites for the adsorption of the gases, (i.e. top of C, top of N, top of Ni) (Fig 5.1(a)) the impurity atom serves as an active site. Since the gas molecules interact near this impurity site, the structural changes in the host system were minimal. As evidenced in Table 5.1, the alterations in bond lengths and angles were insignificant. For CO, NO, and NH_3 adsorption, the adsorption energies were -3.11 eV, -3.15 eV, and -2.07 eV, respectively. These negative values indicate exothermic reactions. As depicted in Fig. 5.2 (a), (d) & (g), the adsorption distances are 1.71 Å, 1.66 Å, and 1.89 Å for CO, NO, and NH_3, respectively. The highly negative adsorption energies suggest strong covalent or chemisorption type interactions.

Table 5.1: Structural parameters, adsorption and electronic properties of Ni decorated α-CN before and after gas adsorption.

System		Bond length (Å)				Angle (°)	d (Å)	E_{ads} (eV)	E_g (eV)
		C-C	N-N	Ni-N	Ni-C				
Ni decorated α-CN	Before adsorption	1.63	2.63	1.89	3.67	$112.00^{(Ni-N-C)}$	--	--	-
	CO	1.63	2.64	2.00	2.90	$111.03^{(Ni-N-C)}$	1.71	-3.11	0.366
	NO	1.63	2.64	2.01	2.90	$111.08^{(Ni-N-C)}$	1.66	-3.15	-
	NH_3	1.63	2.64	1.90	2.83	$112.26^{(Ni-N-C)}$	1.89	-2.07	0.317

As shown in Table 5.1, the Ni-decorated α-CN, initially an extrinsic semiconductor with an intermediate band at the Fermi level (refer to section 3.1), experiences a very narrow band gap opening of 0.366 eV and 0.317 eV upon CO and NH_3 adsorption, respectively. However, with NO adsorption, the intermediate band remains similar to its pre-adsorption state (see Fig. 2(e)). Hybridization of N(NO)-2p, O-2p, Ni-3d, N-2s, C-2s leads to strong covalent interaction between the system and the NO gas. (See fig 5.2 (f)) According to the analysis of partial density of state plots of CO gas adsorbed over Ni decorated α-CN, the 3d orbitals of Ni overlap with the 2p orbitals of C and O from CO, resulting in a covalent bond formation with the host system. At the Fermi level, the 3d orbitals of Ni have the highest contribution, indicating a strong binding between Ni and α-CN (See fig 5.2 (c)).For NH_3 adsorption, the 4p orbitals of Ni overlap with the 2p orbitals of N from NH_3, also indicating a covalent interaction [35].

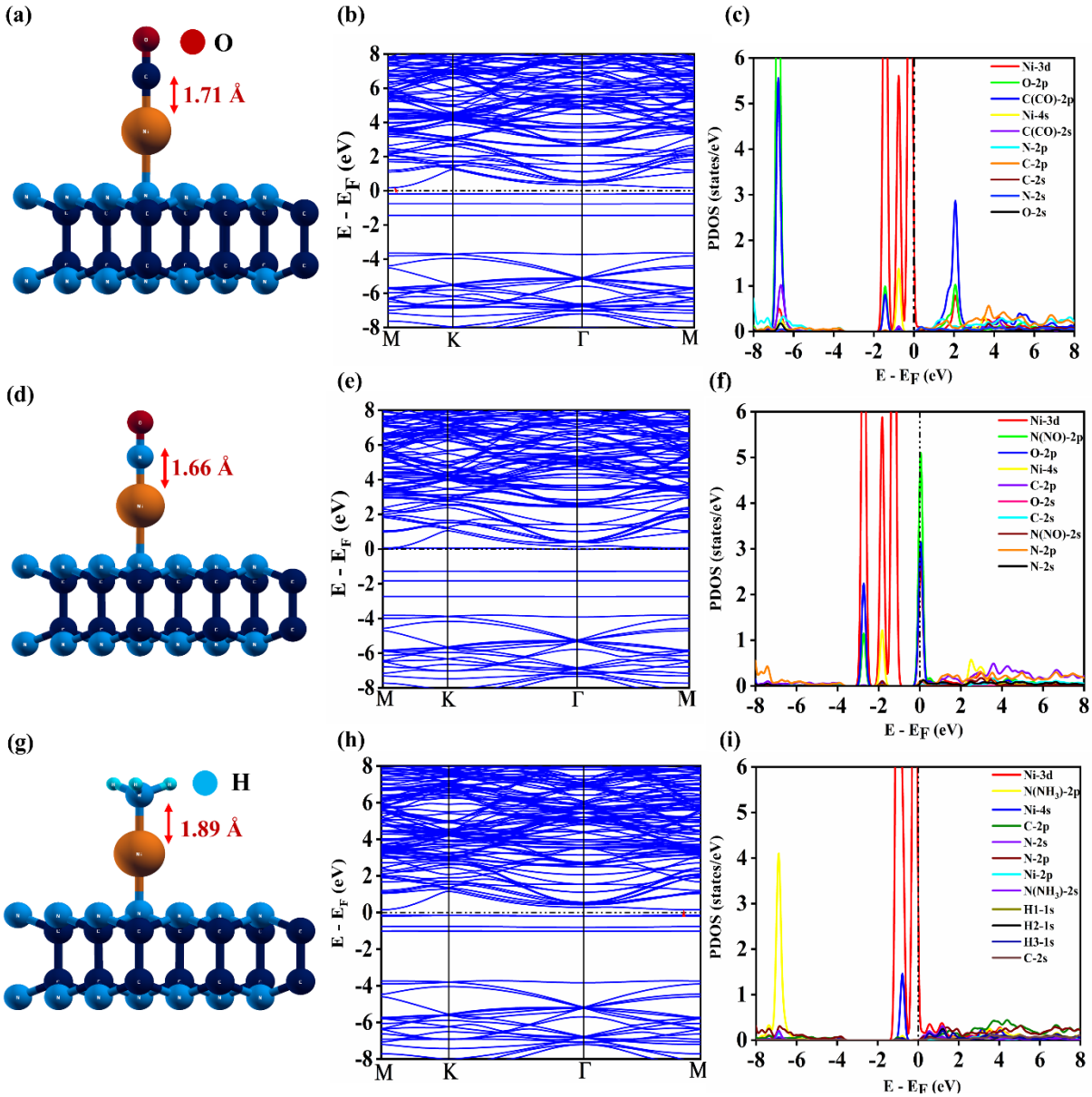

Figure 5.2: Minimum energetic configuration (a), (d), (g); band structure (b), (e), (h); and PDOS (c), (f), (i) of CO, NO, NH_3 gas adsorbed on Ni decorated α-CN respectively.

The 3d orbitals of Ni continue to have the highest contribution at the Fermi level. The band structure plots can be seen in Fig. 5.2 (b, e, h), and the projected density of states (PDOS) plots are shown in Fig. 5.2 (c, f, i) for CO, NO, and NH_3 adsorption, respectively.

In a nutshell, the highly negative adsorption energies attribute to the chemisorption type interaction, which can be corroborated from the formation of the intermediate bands at the Fermi level in the band diagram. In the structural diagrams, one can clearly see the formation of covalent bonds upon the adsorption. The overlapping of orbitals in the PDOS plots, point out to the covalent type interaction as well.

5.3.3. Charge transfer analysis

Charge dynamics play a crucial role in comprehending the sensing mechanics of the adsorbate since the adsorption energy depends on the nature of the bond and the charge exchange between the adsorbate and adsorbent. To understand the detection mechanism of a gas molecule on a Ni-decorated α-CN, the charge of the gas molecule both before and after adsorption was assessed. Table 5.2 presents the Löwdin charge values on gas molecules before and after the adsorption. As one can see, the charges on the CO, NO, and NH_3 gas molecules, increase by 0.1604 e, 0.2791 e, and 0.1120 e, respectively upon the adsorption. While charge on the impurity atom (Ni), decreases by 0.0101 e, 0.1592 e, and 0.0043 e after CO, NO, and NH_3 adsorption, respectively. As demonstrated by charge difference values, the charge transfer takes place mostly between the impurity atom and the gas molecules. This observation is further supported by the charge density diagrams (CDD) in Fig. 5.3, which clearly show changes in charge density distributions in the vicinity of the impurity atom and gas molecules, rather than the monolayer. In these diagrams, cyan regions represent charge accumulation, while yellow regions indicate depletion.

Table 5.2: Löwdin charge values on gas molecule before and after adsorption

Gas molecule	Charge on the isolated molecule (e)	Charge after the adsorption over Ni decorated α-CN (e)	|Δq| (e)
CO	9.9017	10.0621	0.1604
NO	10.916	11.1951	0.2791
NH_3	7.9068	8.0188	0.1120

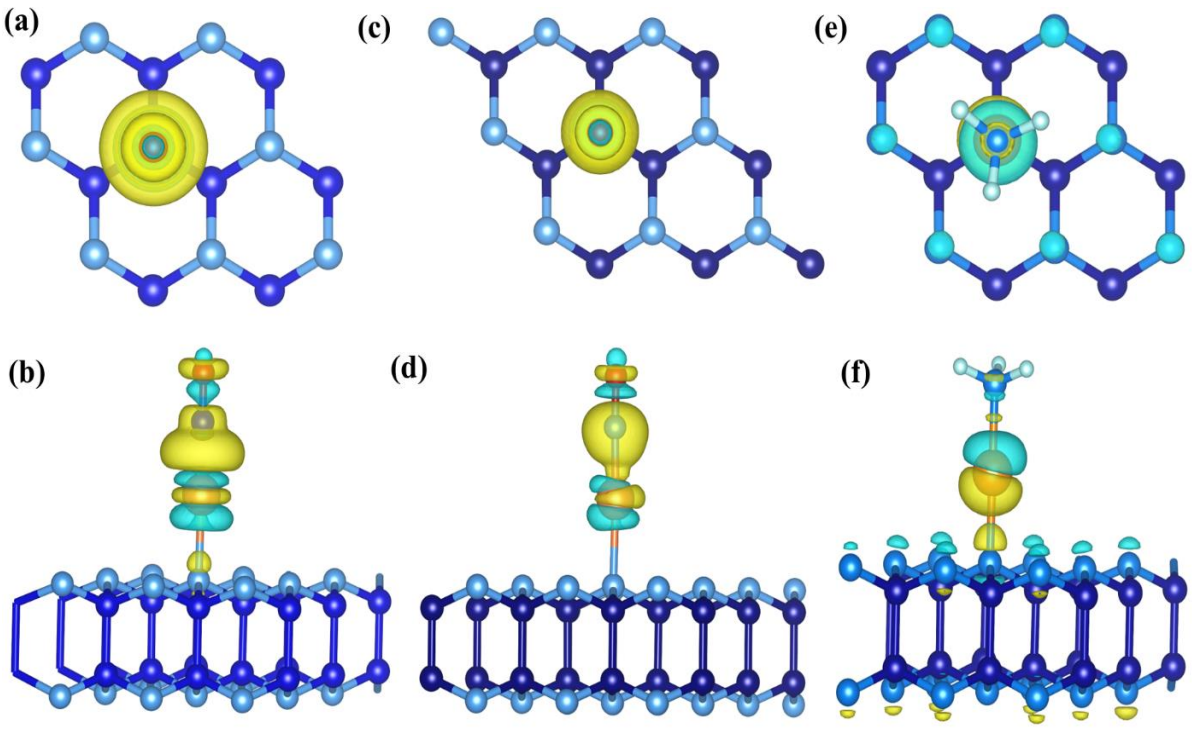

Figure 5.3: Top (a), (c), (e) and side (b), (d), (f) view of charge density difference diagram of CO, NO, NH_3 gas adsorbed over Ni decorated α-CN respectively

5.3.4. Electrical Conductivity

The changes in electronic properties leads to the variations in electrical conductivity. Here we performed electrical conductivity calculations using the BoltzTraP code [31]. The relationship between electrical conductivity and temperature of a material depends on its type. Semiconductors do not have free carriers at 0 K because their valence electrons are tightly bound. When the temperature rises, the covalent bonds in the semiconductor crystal structure begin to break due to the increased energy, generating free electrons and holes. Nearby electrons fill these holes, enabling electron movement and flow, thus increasing the conductivity of semiconductor [32].

For α-CN, as a semiconductor, its conductivity is expected to increase with temperature. However, the extrinsic form of α-CN exhibits some metallic behavior [25,36]. The relaxation time for Ni decorated α-CN should be determined as a function of temperature (T) to establish the exact relationship between conductivity and temperature.

Table 5.3: Variation in σ/τ values upon gas adsorptions at T = 300 K

System	σ/τ (Ωm/s)	Δ(σ/τ)
Ni decorated α-CN	7.50×10^{17}	-
CO adsorbed Ni decorated α-CN	4.50×10^{15}	-7.45×10^{17}
NO adsorbed Ni decorated α-CN	2.50×10^{18}	1.75×10^{18}
NH_3 adsorbed Ni decorated α-CN	1.01×10^{16}	-7.39×10^{17}

Table 5.3 shows the σ/τ values of various gases adsorbed over Ni decorated α-CN. Table 5.3 also presents $\Delta(\sigma/\tau) = \sigma/\tau_{[system+gas]} - \sigma/\tau_{[system]}$. These Δ(σ/τ) values are much higher than that the error due to the unconverged K-mesh grid. Here negative sign determines decrement in the electrical conductivity value after the adsorption of the gas. Fig. 5.4(a), (b) and (c) respectively shows the conductivity plot of CO, NO, and NH_3 gas adsorbed on Ni decorated α-CN. Based on our calculations in Table 5.3, the electrical conductivity relative to relaxation time (σ/τ) slightly increases with temperature. At 300 K, the Δ(σ/τ) value decreases by 7.45×10^{17} Ωm/s and 7.39×10^{17} Ωm/s, for CO and NH_3 adsorptions, respectively. Whereas for NO adsorption, it increases by 1.75×10^{18} Ωm/s. Fig. 5.4 conveys the same sentiment graphically. The increment in the conductivity is attributed to increment of states over E_F with more states occurring due to NO gas. The gap between the curves before and after adsorption is significantly wider for CO compared to NO or NH_3 adsorption, indicating a change in electrical conductivity upon adsorption[37]. Typically, large amount of charge transfer attributes to high sensitivity in the predicted device[38]. However, in our cases, the charge transfer is noticeable but not large in magnitude. Thus, it is obvious that the observed change in the conductivity solely points out to the strong chemisorption type interaction.

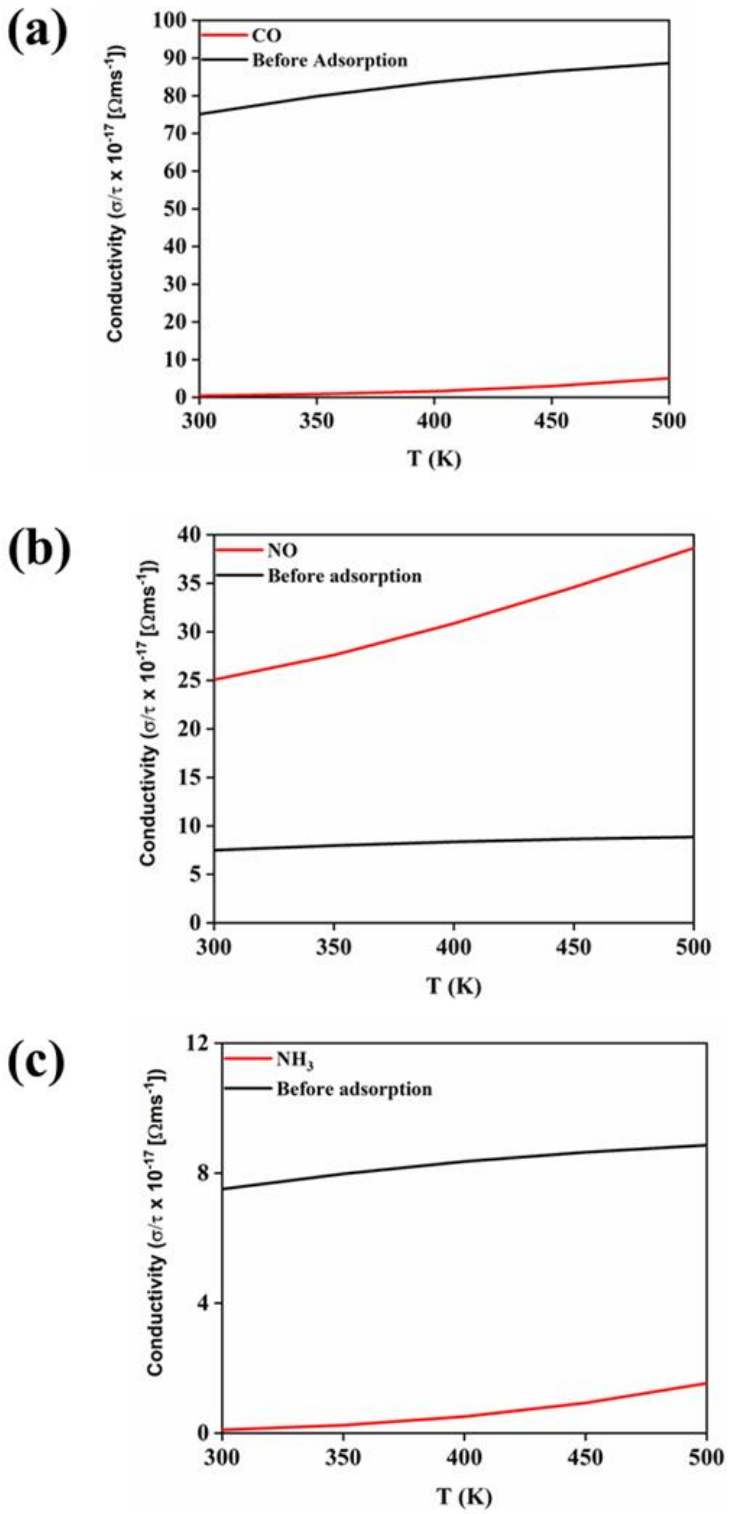

Figure 5.4: Graphical representation of Δσ/τ ratio with respect to the temperature.

5.3.5. Work function Analysis

The Fermi level and work function (ϕ) of a material are influenced by gas adsorption, making it essential to examine key components for a ϕ-type sensor. A Kelvin oscillator instrument is used in ϕ-type sensors to estimate ϕ-values before and after gas molecule adsorption. When the sensor's work function changes due to gas adsorption, the gate voltage is disrupted, generating an electrical signal. The work function (ϕ) is defined as the minimum energy required to remove an electron from a material to a point in the vacuum just outside the solid surface, as given by the following equation [3]:

$$\varphi = E_{vac} - E_F \text{ ---- (2)}$$

Where E_{vac} is the energy at the vacuum (i.e. at the interface), E_F is the energy at Fermi level. The variation in the value of φ of an adsorbent system during gas adsorption process changes its field emission characteristics, which can be correlated using a classical Richardson-Dushman equation. The field emission current density for electron in vacuum is given by Richardson-Dushman equation [39]:

$$j = AT^2\exp(-\varphi/kT) \text{ ----- (3)}$$

Where A stands for Richardson constant (A/m^2) and T is the absolute temperature. As shown in Table 5.4, work function decreases substantially in the adsorption of all three gases. The decrement is highest in the case of CO adsorption though (56.5%) and lowest in the case of NH_3 adsorption (18.5%). Suggesting that Ni decorated α-CN can be used as φ-type sensor for all three gases. Fig. 5.5 shows the work function plots for Ni decorated α-CN before and after the gas adsorption.

Table 5.4: Comparative work function analysis

Configuration		E_{vac} (eV)	E_F (eV)	φ (eV)	Δφ
Ni decorated α-CN	Before adsorption	5	1.76	3.24	-
	CO	5.07	3.66	1.41	-56.5%
	NO	5.12	3.36	1.76	-45.7%
	NH_3	5.28	2.64	2.64	-18.5%

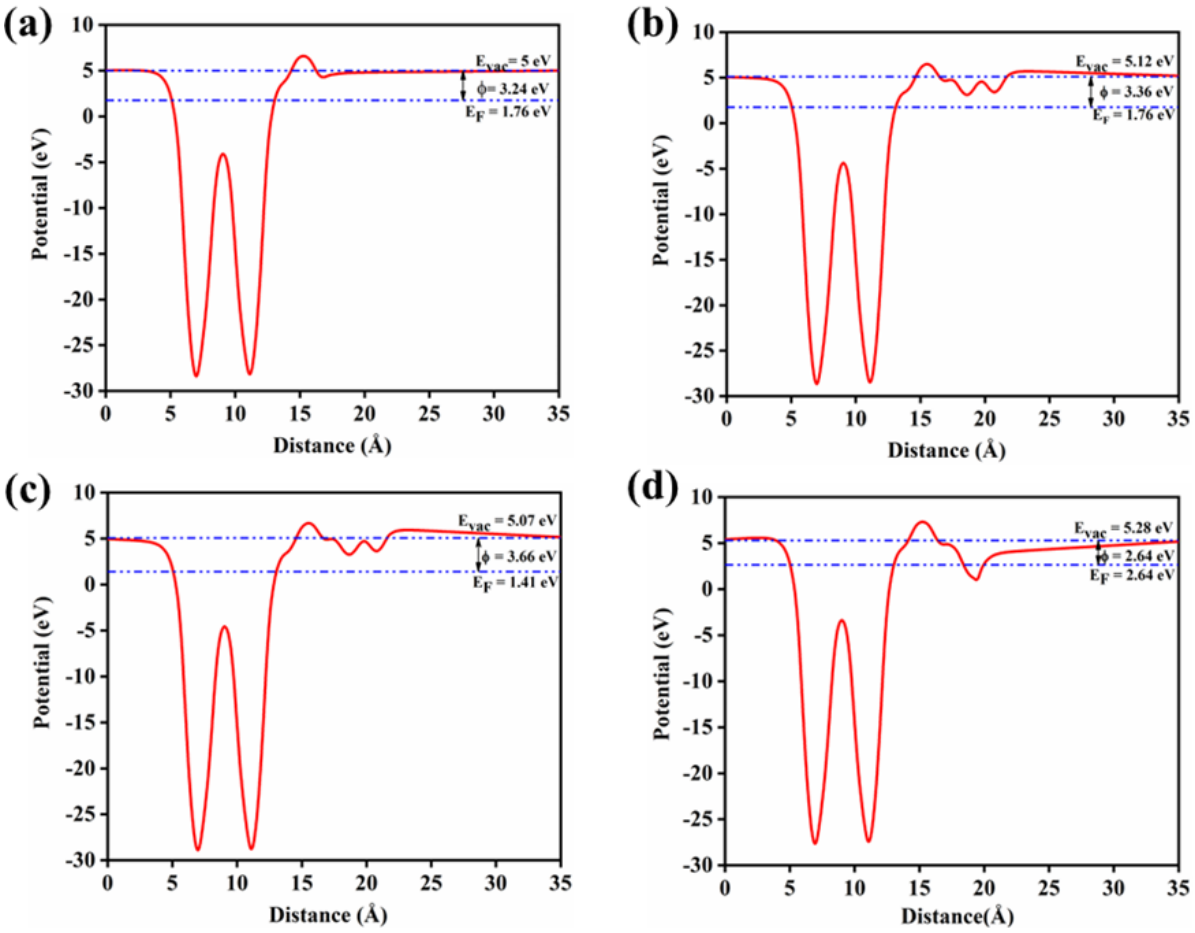

Figure 5.5: Work functions plots of (a)Ni decorated (b) CO adsorbed (c) NO adsorbed (d) NH_3 adsorbed α-CN

5.3.6. Recovery Time

In the devices for gas sensing, the recovery time (τ) is another key aspect. It determines how simple or complex the desorption process is, with the estimation of desorption time [40]. It should be faster if we need the material to perform as a sensor [41]. In the case of sensor materials, strong interactions with gases should be avoided since they make it more difficult for the gas molecules to dissociate and cause the longer recovery time. τ is given by [42]:

$$\tau = \upsilon^{-1} \exp\left(-\frac{E_{ad}}{KT}\right) \text{ ----- (4)}$$

We have considered the attempt frequency υ = 10^{12} s^{-1} (for IR radiation) and absolute temperature T = 300 K (see Table 5). If the computed recovery time prolong more than several hours, rather than sensing or detection, the material is more suitable for toxic gas removal

applications [39]. As one can see the shortest recovery time being 2.2478×10^{32} seconds, which is for the case of NH_3 adsorption. As the τ values are extremely long (exceeding several hours), for all three adsorptions, one can safely conclude that the Ni decorated α-CN is more suitable for the removal purposes of CO, NO and NH_3 gases, from specific environments[1].

In other words, the prolonged recovery times are due to the highly negative adsorption energies which indicate the chemisorption type interaction. The structural diagrams and PDOS plots point out the covalent bond formation between the gas molecules and the host system. The strong interaction can also be validated by the formation of intermediate bands at the Fermi level in the band structure. As per our discussion in the previous section, the large changes in work functions impute the use of Ni decorated α-CN as a ϕ-type sensor, but the low sensitivity for the predicted device and longer recovery times rule out that possibility.[43] However this is not the bottleneck for the removal applications [39].

Table 5.5: Recovery times for CO, NO, and NH_3 adsorption

System	Gas	τ (s)
Ni decorated α-CN	CO	1.7689×10^{40}
	NO	8.3117×10^{40}
	NH_3	2.2478×10^{32}

5.3.7. Comparison of the adsorption performance of Ni decorated monolayer with previously reported α-CN and other transition metal-functionalized nanomaterials

As per the discussion of the previous sections, the Ni decorated α-CN is suitable for removal of CO, NO, and NH_3 gases rather than sensing. This is inferred from the values of adsorption energies and consequent recovery times. Table 5.6 shows the calculated adsorption properties of Ni decorated monolayer with α-CN and previously reported other transition metal-functionalized nanomaterials. Evidently, the adsorption energies are most negative for the NO and NH_3 adsorptions as compared to previously reported studies. The table below shows where our study stands, as compared to the reported data.

Table 5.6: Adsorption properties of Ni decorated monolayer with previously reported α-CN and other transition metal-functionalized nanomaterials

System	CO adsorption		NO adsorption		NH_3 adsorption		Ref.
	E_{ad} (eV)	d (Å)	E_{ad} (eV)	d (Å)	E_{ad} (eV)	d (Å)	
Ni decorated α-CN	-3.11	1.71	-3.15	1.66	-2.07	1.89	This work
Pristine α-CN	-0.08	3.11	-0.07	3.00	-0.28	2.73	24
Al doped α-CN	-0.88	2.00	-1.89	1.77	-	-	25
C defected α-CN	-3.63	0.78	-1.90	1.77	-	-	
Cr doped C_9N_4	-2.07	-	-3.05	-	-1.76	-	44
Ag doped h-BN	-	-	-0.82	-	-	-	
Ni embedded MoS_2	-1.42	1.69	-1.69	1.88	-1.13	1.33	45
Ni doped graphene	-1.02	1.89	-	-	-	-	46
Ni doped g-C_3N_4	-2.13	-	-	-	-	-	47

5.4. Conclusion

In this chapter, we examined the adsorption performance of an α-CN monolayer decorated with Ni atom for CO, NO, and NH_3 gases. In its stable structure, the Ni atom forms a bond with the nitrogen in α-CN, with a bond length of 1.63 Å. Since the impurity binds to the surface, the lattice parameter of α-CN remains unchanged. The Ni-decorated α-CN becomes an extrinsic semiconductor due to the formation of an intermediate band at the Fermi level, resulting in the absence of a band gap. However, upon adsorption of CO and NH_3, a slight band gap opens (0.366 eV and 0.317 eV, respectively).

The PDOS plots qualitatively and the charge transfer analysis quantitatively demonstrate the strong interaction between the gas molecules and the host system. The relatively small positive charge transfer indicates low sensitivity of the predicted device. Therefore, the changes in conductivity after the adsorption process solely point to strong interaction. The work function (ϕ) significantly decreased after the adsorption of the gases, suggesting potential for ϕ-type sensor applications. However, the low sensitivity and longer recovery times (exceeding several hours) rule out this possibility. In conclusion, Ni-decorated α-CN is more suitable for the removal of CO, NO, and NH_3 gases rather than their detection.

BIBLIOGRAPHY:

[1 S. Vadalkar, D. Chodvadiya, N. N. Som, K. N. Vyas and P. K. Jha, *ChemistrySelect*, 2023, **8**, e202204862.

2 P. Lung and C. Mol, *Am. J. Physiol.*, 2003, **C**, 1–32.

3 D. Upadhyay, B. Roondhe, A. Pratap and P. K. Jha, *Appl. Surf. Sci.*, 2019, **476**, 198–204.

4 Y. Kojima, *Int. J. Hydrogen Energy*, 2024, **50**, 732–739.

5 Y. Peng and J. Li, *Front. Environ. Sci. Eng.*, 2013, **7**, 403–411.

6 G. L. Li, Y. Sui, M. Dong, W. L. Ye, C. T. Zheng and Y. D. Wang, *Appl. Phys. B Lasers Opt.*, 2015, **119**, 287–296.

7 P. K. Narayan, *Appl. Econ.*, 2005, **37**, 1063–1071.

8 A. K. Geim and K. S. Novoselov, *Nat. Mater.*, 2007, **6**, 183–191.

9 S. Yang, C. Jiang and S. huai Wei, *Appl. Phys. Rev.*, 2017, 4.

10 X. Liu, T. Ma, N. Pinna and J. Zhang, *Adv. Funct. Mater.*, , DOI:10.1002/adfm.201702168.

11 X. Tang, A. Du and L. Kou, *Wiley Interdiscip. Rev. Comput. Mol. Sci.*, 2018, **8**, 1–18.

12 W. Wang, Y. Zhang, C. Shen and Y. Chai, *AIP Adv.*, , DOI:10.1063/1.4942491.

13 Z. Bo, X. Guo, X. Wei, H. Yang, J. Yan and K. Cen, *Phys. E Low-Dimensional Syst. Nanostructures*, 2019, **109**, 156–163.

14 X. Zhou, W. Chu, Y. Zhou, W. Sun and Y. Xue, *Appl. Surf. Sci.*, 2018, **439**, 246–253.

15 H. Baccar, A. Thamri, P. Clément, E. Llobet and A. Abdelghani, *Beilstein J. Nanotechnol.*, 2015, **6**, 919–927.

16 Y. Fan, J. Zhang, Y. Qiu, J. Zhu, Y. Zhang and G. Hu, *Comput. Mater. Sci.*, 2017, **138**, 255–266.

17 H. Wei, Y. Gui, J. Kang, W. Wang and C. Tang, *Nanomaterials*, 2018, **8**, 1–12.

18 K. Ma, Y. Wang, Y. Zheng, J. Xiao, L. Xu, X. Dai and Z. Wang, *Phys. E Low-*

Dimensional Syst. Nanostructures, 2022, **142**, 4–7.

19 S. Li, X. Wei, S. Zhu, Q. Zhou and Y. Gui, *Vacuum*, 2021, **187**, 22–25.

20 J. Wang, Q. Zhou and W. Zeng, *Appl. Surf. Sci.*, 2019, **479**, 185–197.

21 J. Lu, X. Zhang, X. Wu, Z. Dai and J. Zhang, *Sensors (Switzerland)*, 2015, **15**, 13522–13532.

22 D. Chodvadiya, N. N. Som, P. K. Jha and B. Chakraborty, *Int. J. Hydrogen Energy*, 2021, **46**, 22478–22498.

23 T. K. Gajaria, D. Chodvadiya and P. K. Jha, *ACS Appl. Nano Mater.*, 2021, **4**, 4474–4483.

24 C. He, M. Zhang, T. T. Li and W. X. Zhang, *Appl. Surf. Sci.*, 2020, **505**, 3–7.

25 H. Mistry, D. Chodvadiya, S. Vadalkar, K. N. Vyas and P. K. Jha, *Surfaces and Interfaces*, 2024, 46.

26 W. Kohn, A. D. Becke and R. G. Parr, *Density Functional Theory of Electronic Structure*, 1996.

27 P. Giannozzi, S. Baroni, N. Bonini, M. Calandra, R. Car, C. Cavazzoni, D. Ceresoli, G. L. Chiarotti, M. Cococcioni, I. Dabo, A. Dal Corso, S. De Gironcoli, S. Fabris, G. Fratesi, R. Gebauer, U. Gerstmann, C. Gougoussis, A. Kokalj, M. Lazzeri, L. Martin-Samos, N. Marzari, F. Mauri, R. Mazzarello, S. Paolini, A. Pasquarello, L. Paulatto, C. Sbraccia, S. Scandolo, G. Sclauzero, A. P. Seitsonen, A. Smogunov, P. Umari and R. M. Wentzcovitch, *J. Phys. Condens. Matter*, 2009, **21**, 44.

28 J. P. Perdew and K. Burke, *Phys. Rev. B - Condens. Matter Mater. Phys.*, 1996, **54**, 16533–16539.

29 J. D. Pack and H. J. Monkhorst, *Phys. Rev. B*, 1977, **16**, 1748–1949.

30 S. K. Jana, D. Chodvadiya, N. N. Som and P. K. Jha, *Diam. Relat. Mater.*, 2022, **129**, 109305.

31 G. K. H. Madsen and D. J. Singh, *Comput. Phys. Commun.*, 2006, **175**, 67–71.

32 N. M. R. Shah, C. D. Yeo, M. Choi, Y. K. Hong and J. H. You, *Nanomanufacturing Metrol.*, 2023, **6**, 1–10.

33 J. Liu, J. Liu, W. Song, F. Wang and Y. Song, *J. Mater. Chem. A*, 2014, **2**, 17477–17488.

34 N. K. Das and T. Shoji, *J. Alloys Compd.*, 2013, **580**, 37–54.

35 B. R. Bhagat and A. Dashora, *Carbon N. Y.*, 2021, **178**, 666–677.

36 P. Patel, S. Patel, D. Chodvadiya, M. H. Dalsaniya, D. Kurzydłowski, K. J. Kurzydłowski and P. K. Jha, *J. Energy Storage*, 2023, **71**, 10–13.

37 R. K. Choudhury, B. R. Bhagat, K. H. Mali, R. Pokar and A. Dashora, *Appl. Surf. Sci.*, , DOI:10.1016/j.apsusc.2022.154426.

38 M. Rostami and A. Moazamigodarzi, *Mater. Today Commun.*, 2024, **38**, 108107.

39 Y. Liu, C. Liu and A. Kumar, *Mol. Phys.*, , DOI:10.1080/00268976.2020.1798528.

40 A. Yadav, *Comput. Theor. Chem.*, , DOI:10.1016/j.comptc.2022.114005.

41 S. Kanti Jana, N. N. Som and P. K. Jha, *J. Mol. Liq.*, 2023, **383**, 1–4.

42 S. Peng, K. Cho, P. Qi and H. Dai, *Chem. Phys. Lett.*, 2004, **387**, 271–276.

43 E. Mohammadi-Manesh, M. Vaezzadeh and M. Saeidi, *Comput. Mater. Sci.*, 2015, **97**, 181–185.

44 Y. Hu, L. Liu, S. Zhang and X. Chen, *Colloids Surfaces A Physicochem. Eng. Asp.*, 2024, **689**, 133716.

45 Y. Fan, J. Zhang, Y. Qiu, J. Zhu, Y. Zhang and G. Hu, *Comput. Mater. Sci.*, 2017, **138**, 255–266.

46 B. Wanno and C. Tabtimsai, *Superlattices Microstruct.*, 2014, **67**, 110–117.

47 H. Basharnavaz, A. Habibi-Yangjeh and M. Pirhashemi, *Chem. Phys. Lett.*, , DOI:10.1016/j.cplett.2020.137676.